ADVANCED FUNCTIONAL MATERIALS
www.afm-journal.de

Efficient Water Splitting System Enabled by Multifunctional Platinum-Free Electrocatalysts

Yaotang Zhong, Yitong Lu, Zhenghui Pan, Jie Yang, Guohao Du, Jiawei Chen, Qiankui Zhang, Hebing Zhou, John Wang, Chunsheng Wang,* and Weishan Li**

Tremendous research efforts have been focused on the development of a water splitting system (WSS) to harvest hydrogen fuels, but currently available WSSs are complicated and cost-ineffective mainly due to the applications of noble platinum or different electrocatalysts. Herein, a novel WSS comprising electricity generation from solar panels, electricity storage in rechargeable zinc–air batteries (ZABs), and water splitting in electrolyzers, enabled by hybrid cobalt nanoparticles/N-doped carbon embellished on carbon cloth (Co–NC@CC) as multifunctional platinum-free electrocatalysts is reported. Consequently, the Co–NC@CC electrode presents excellent trifunctional electrocatalytic activity with an onset potential of 0.94 V for oxygen reduction reaction, and an overpotential of 240 and 73 mV to achieve a current density of 10 mA cm^{-2} for oxygen and hydrogen evolution reactions, respectively. For a proof-of-concept application, a rechargeable ZAB assembled from the high-performance Co–NC@CC air cathode exhibits a high open circuit potential of 1.63 V and a superior energy density of 1051 Wh kg$^{-1}_{Zn}$. Furthermore, an overall water splitting electrolyzer constructed by the symmetrical Co–NC@CC electrodes delivers a current density of 10 mA cm^{-2} at a low cell voltage of 1.57 V. Such a solar-powered WSS can harvest hydrogen day and night, demonstrating a potential for application in sustainable renewable energy.

Dr. Y. Zhong, Dr. Y. Lu, Dr. G. Du, Dr. J. Chen, Dr. Q. Zhang, Prof. H. Zhou, Prof. W. Li
School of Chemistry
South China Normal University
Guangzhou 510006, China
E-mail: liwsh@scnu.edu.cn

Dr. Y. Zhong, Dr. J. Chen, Dr. Q. Zhang, Prof. H. Zhou, Prof. W. Li
National and Local Joint Engineering Research Center of MPTES in High Energy and Safety LIBs
Engineering Research Center of MTEES (Ministry of Education), and Key Lab. of ETESPG (GHEI)
South China Normal University
Guangzhou 510006, China

Dr. Z. Pan, Dr. J. Yang, Prof. J. Wang
Department of Materials Science and Engineering
National University of Singapore
Singapore 117574, Singapore
E-mail: msepz@nus.edu.sg

Prof. C. Wang
Department of Chemical and Bimolecular Engineering
University of Maryland
College Park, MD 20740, USA
E-mail: cswang@umd.edu

The ORCID identification number(s) for the author(s) of this article can be found under https://doi.org/10.1002/adfm.202009853.

DOI: 10.1002/adfm.202009853

1. Introduction

Hydrogen is the cleanest energy in the world and its efficient preparation will determine the sustainability of our society.[1–5] A water splitting system (WSS), which uses renewable energy such as solar energy to generate electricity and rechargeable batteries to store electricity, is a promising strategy to efficiently harvest hydrogen.[6] However, currently available WSSs require platinum (Pt) or Pt-like noble metal electrocatalysts for oxygen reduction reaction (ORR) on the cathode in batteries, as well as oxygen evolution reaction (OER) on the anode and hydrogen evolution reaction (HER) on the cathode in electrolyzer, leaving a challenging issue of their high costs.[7] State-of-the-art electrocatalysts such as Pt are highly efficient for HER and ORR, whereas IrO_2 and RuO_2 favor OER. The nobility of Pt, Ir, Ru, and the requirement of multiple electrocatalysts for OER, ORR, and HER add much cost to the WSS assembly, restricting the application of WSSs in large scale.

In recent decades, non-noble transition metals (e.g., Fe, Co, Ni, and Mo) and their compounds (oxides, sulfides, carbides, nitrides, phosphides, and alloys) have been considered as the promising Pt-free electrocatalysts simultaneously for OER, ORR, and HER of WSS on account of their high activity and low-cost.[7–13] For example, Yin et al.[7] synthesized cobalt (Co)–nickel sulfide nanowires enriched with oxygen vacancies (NiS_2/CoS_2–O NWs) as trifunctional electrocatalysts for OER, ORR, and HER to achieve high-performance WSS, with an overpotential of 235 mV (vs standard oxygen potential, 1.23 V) to achieve a current density of 10 mA cm^{-2} for OER, which was among the best OER electrocatalysts reported so far. Amiinu et al.[13] reported a trifunctional electrocatalyst comprising MoS_2 nanosheet vertically arrayed on Mo–N/C framework (Mo–NC@MoS_2) with an overpotential of 117 mV (vs standard hydrogen potential, 0 V) at a current density of 10 mA cm^{-2} for HER, much lower than the majority of MoS_2-based electrocatalysts reported. However, these trifunctional electrocatalysts were highly active toward only one reaction, but not so active for other reactions, which mitigates the overall efficiency of WSSs. Recently, Pei et al.[8] demonstrated a trifunctional electrocatalyst made of Co nanoparticles anchored on a N-doped graphene (NG) modified carbon foam (CF) framework for WSS. The mixed-covalent

Co nanoparticles (metallic Co and its oxides) are simultaneously beneficial for OER, ORR, and HER, with their activity and stability being greatly enhanced by coupling with the NC.[14–17] However, the configuration of this multifunctional electrocatalyst presents a low mass loading of active material (1.0 mg cm^{-2}), greatly limiting the efficiency of WSSs.

In this work, we propose a facile two-step route to synthesize a novel Pt-free multifunctional electrocatalysts for WSS, including the precursor growth of 2D micron-sized Co-based metal–organic framework on the fibers of carbon cloth (Co-MOF@CC) and the subsequent carbonization process of obtaining Co nanoparticles anchored into N-doped carbon microarrays (Co–NC@CC). It is noteworthy that the free-standing Co–NC@CC electrode is fabricated without any structure-directed and binder agent, which features a high mass loading of active material (3.0 mg cm^{-2}) and an ability to prevent the aggregation of Co nanoparticles, thus resulting in superior activity and stability simultaneously for OER, ORR, and HER compared to the recently reported free-standing electrodes.[7–9,16] For ORR, the well-prepared Co–NC@CC exhibits an ultrahigh limiting current density of 28.5 mA cm^{-2} at 1600 rpm, which is the highest reported to date. For OER, the Co–NC@CC delivers a low overpotential of 240 mV (vs standard oxygen potential) to achieve a current density of 10 mA cm^{-2}, close to the best OER electrocatalyst (235 mV) reported previously.[7] And for HER, the Co–NC@CC only requires a low overpotential of 73 mV (vs standard hydrogen potential) for a current density of 10 mA cm^{-2}, far below than that of most Co-based electrocatalysts reported in alkaline media.[8,9]

For a proof-of-concept application, the trifunctional electrocatalytic activities and stabilities of Co–NC@CC electrode enable an overall water splitting electrolyzer (WSE) driven by two as-assembled zinc–air batteries (ZABs) and a polycrystalline Si solar panel (PSSP). Such a novel WSS can harvest energy from sunlight without an external power source and operate overall water splitting throughout day and night. Thus, the present study develops a simple and facile synthetic route of fabricating cost-effective and highly efficient multifunctional electrocatalysts for WSS, enormously boosting the sustainable development of green and renewable energy systems.[18]

2. Results and Discussion

The two-step synthetic route of the free-standing Co–NC@CC electrode is shown schematically in **Figure 1**a, and the microstructure of the as-synthesized samples at each step was visualized by the scanning electron microscopy (SEM) and transmission electron microscopy (TEM). First, 2D-leaflike microarrays are interlaced grown on the fibers of carbon cloth (Co-MOF@CC) through a facile solution method. As depicted in Figure 1b,c, the Co-MOF is compactly embellished on CC, with the size of ≈2 µm. And subsequently, the Co-MOF@CC was processed by a reduction carbonization at different temperatures (Figure S1, Supporting Information), during which the organic ligands and Co ions in Co-MOF are transformed into porous NC and metallic Co nanoparticles, respectively. Figure 1d,e describes that the well-prepared Co–NC@CC sample (the Co-MOF@CC pyrolyzed at 750 °C for 2 h, denoted as Co–NC-750 °C) possesses an angular morphology with rough surface, within which the embedded Co nanoparticles with diameters of ≈20 nm (the inset of Figure 1f) are uniformly scattered. Meanwhile, the as-formed Co nanoparticles can be exactly detected by X-ray diffraction (XRD) pattern, and all diffraction are perfectly consistent with the Co phase (JCPDS #15-0806) (Figure S2, Supporting Information). Additionally, the high-resolution TEM (HRTEM) image and the corresponding selected area electron diffraction (SAED) image (Figure 1f,g) identify *d*-spacing values of 0.177 and 0.205 nm in a higher-contrast nanoparticle, assigned to the (200) and (111) crystal planes of the metallic Co species, respectively. And the lattice fringe spacing of ≈0.34 nm is referred to the (002) crystal plane of graphitized carbon around Co nanoparticles.[8] The specific surface area (62 m^2 g^{-1}) and average pore (4.1 nm) of the Co–NC-750 °C were further evaluated by Brunner–Emmett–Teller (BET) tests (Figure S3, Supporting Information). Such a highly porous structure with large specific surface area greatly guarantees the high electroactive surface area and efficient mass transport of the Co–NC electrocatalysts.[19–21]

To take further insights into the chemical states and molecular structures, the Co–NC@CC-series samples pyrolyzed at different temperatures were then studied by Raman spectra and X-ray photoelectron spectroscopy (XPS). As shown in **Figure 2**a, all the samples visibly reveal the characteristic D band (1347 cm^{-1}) and G band (1595 cm^{-1}) of carbon in Raman spectra, emanating from the disordered carbon and the crystallized graphitic carbon, respectively. With an increase in pyrolysis temperature, the I_D/I_G intensity ratio decreases from 1.01 to 0.87. Correspondingly, the electrical resistivity decreases from 443 to 155 mΩ cm^{-2} (Figure S4, Supporting Information). These results suggest a higher degree of graphitization and an enhanced electrical conductivity of the as-obtained carbon framework by high-temperature carbonization.[22] In addition, two weak Raman peaks appeared at 475 and 678 cm^{-1} can also be observed in all samples, which respectively refer to the E_g and A_{1g} modes of CoO.[8] However, in combination of the metallic Co phase from XRD results (Figure S2, Supporting Information), these peaks imply that the surface of Co particles is partially oxidized. For XPS, Figure 2b depicts that the N 1s spectrum of all samples can be deconvoluted into four typical bonding peaks including pyridinic N (398.6 eV), pyrrolic N (399.5 eV), graphitized N (400.8 eV), and oxidized N (403.2 eV).[23] Notably, as the pyrolysis temperature increases, the N content in Co–NC@CC samples (Table S1, Supporting Information) gradually decreases from 12.6 to 6.7 At% (At%, atomic ratio). Among them, the content of pyridinic, pyrrolic, and oxidized N decreases, whereas the content of graphitized N increases, which can be attributed to a higher thermal stability of the graphitized N compared to the other three N species.[8] Furthermore, as Figure 2c illustrates, the different N species and O atoms incorporated with C could break the electronic neutrality of the carbon framework and thereby facilitate the electrocatalytic processes.[19,24,25] And the high-resolution XPS spectra of O 1s (Figure S5, Supporting Information) further confirm the existence of oxygen functional groups with the Co—O, C=O, and C—O bonds. The 2p level scan of Co (Figure 2d) indicates two chemical states of the containing

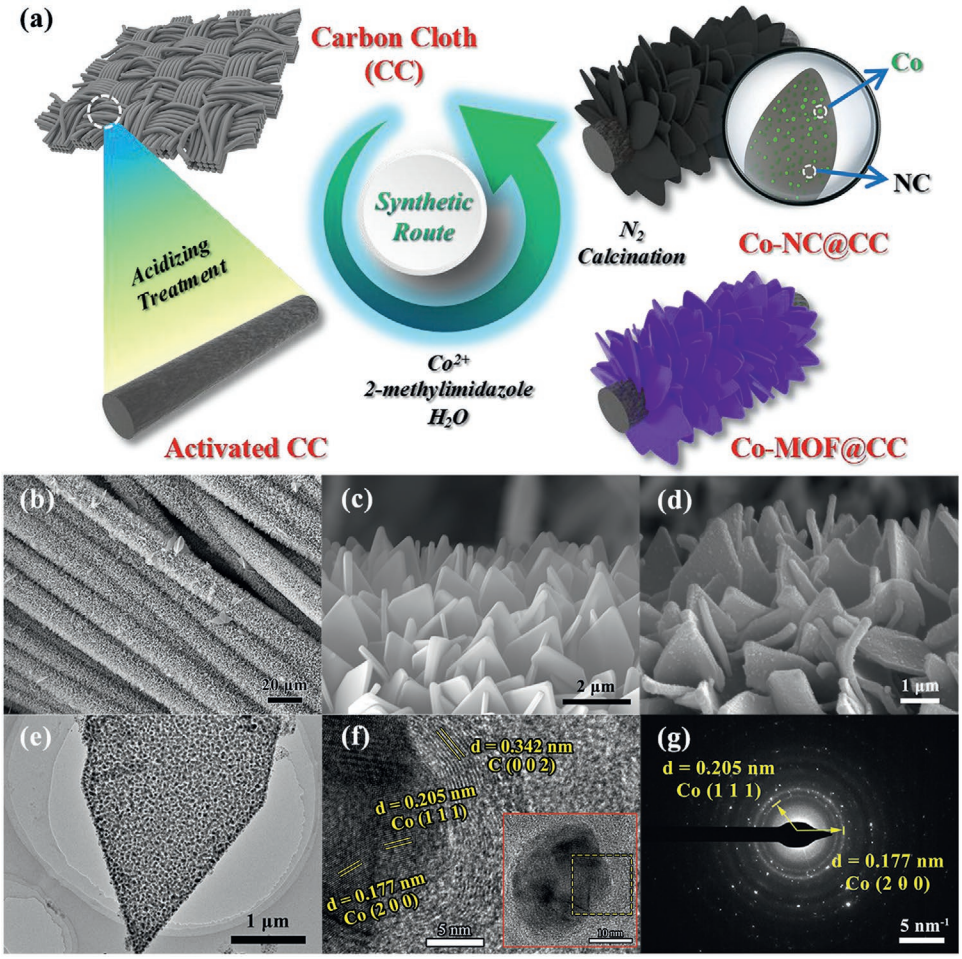

Figure 1. Synthesis and structural characterization of Co–NC@CC. a) Schematic illustration on the synthetic route of Co–NC@CC. b,c) SEM images of Co-MOF@CC sample at different magnifications. d,e) SEM and TEM images of Co–NC-750 °C sample. f,g) HRTEM image and the corresponding SAED image of Co–NC-750 °C sample. The inset of (f) shows the diameter of a Co nanoparticle which is ≈20 nm.

Co atoms: metallic Co (778.56 and 793.45 eV) and Co^{2+} species (780.51 and 795.86 eV),[26–28] which are consistent with the Raman and XRD results. The Co^{2+} species mainly consist of a small amount of CoO formed on the surface of metallic Co and the complexes coordinated by Co^{2+} ions and imidazole ligands residual from the pristine Co-MOF precursor. As expected, the Co^{2+} species in Co bulk seem to be progressively transformed into metallic Co species with temperatures rising, suggesting that higher oxidation state Co^{2+} species would be gradually reduced by higher pyrolysis temperature. In particular, this mixed-covalent Co species (metallic Co and its oxides) not only are beneficial for the processes of multiple electrochemical redox reactions, but also show a synergic effect when coupling with NC, which would greatly guarantee the activity of hybrid Co–NC electrocatalysts toward ORR, OER, and HER.

ORR is an important cathode reaction of fuel cells and metal–air batteries.[29–32] The electrocatalytic activity of the Co–NC electrocatalysts toward ORR was first investigated by linear sweeping voltammetry (LSV) in 1 M oxygenated potassium hydroxide solution (KOH), within the potential range from 0.2 to 1.1 V at a scan rate of 5 mV s^{-1} (the experimental detail can be found in Figure S6, Supporting Information). As a contrast, the samples of commercial Co, Pt/C, and hybrid IrO_2 + Pt/C (weight ratio is 1:1) were studied as well. Strikingly, as shown in **Figure 3**a, the Co–NC-750 °C exhibits a limiting current density of 28.5 mA cm^{-2} and an onset potential of 0.94 V with a half-wave potential of 0.81 V, which is superior to that of the state-of-the-art Pt/C (a limiting current density of 26.5 mA cm^{-2} and an onset potential of 0.94 V with a half-wave potential of 0.73 V), as well as significantly outperforming those of other comparative samples. This excellent performance can be attributed to the higher BET active surface (62 m^2 g^{-1}) and suitable pore diameter (4.1 nm) of Co–NC-750 °C, compared with Pt/C (7 m^2 g^{-1} and 2.2 nm, Figure S7, Supporting Information) and the Co–NC@CC samples annealed at other temperatures (32 m^2 g^{-1} and 3.3 nm for Co–NC-550 °C; 51 m^2 g^{-1} and 3.6 nm for Co–NC-650 °C; and 33 m^2 g^{-1} and 4.8 nm for Co–NC-850 °C, Figure S3, Supporting Information), which contribute synergistically to oxygen-adsorption and oxygen-reduction process, thus boosting ORR activity. Also, the high content of pyridine-N (4.74 At%) and graphitic-N (3.49 At%) species in Co–NC-750 °C could facilitate the adsorption of reductive O_2 and promote electron transfer from the electronic bands of carbon to the antibonding orbitals of O_2, respectively,[33,34] which

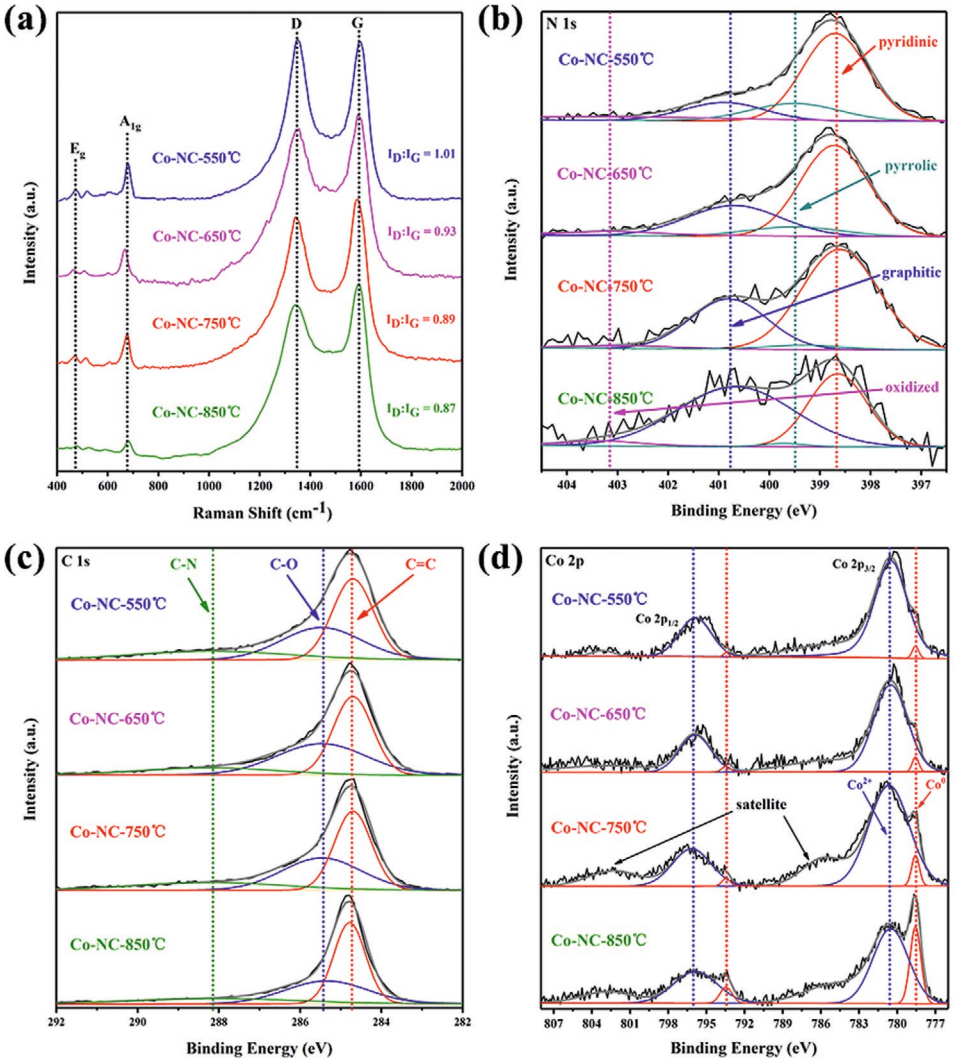

Figure 2. Chemical states and molecular structures of Co–NC@CC. a) Raman spectra of the Co–NC@CC-series samples pyrolyzed at different temperatures. The high-resolution XPS spectra of b) N 1s, c) C 1s, and d) Co 2p of the Co–NC@CC-series samples.

further improve the ORR activity. The calculated ORR faradaic efficiency of Co–NC-750 °C is ≈97.37% at 0.30 V (Table S2, Supporting Information). In addition, the corresponding Tafel slope of Co–NC-750 °C is 76 mV dec^{-1} and even lower than that of Pt/C (88 mV dec^{-1}) (Figure 3b), further signaling its favorable ORR kinetics. It is highlighted that the N-doped 3D porous array architecture with abundant electroactive sites is beneficial for the reinforcing oxygen-adsorption, rapid electron-transfer and efficient ion-diffusion.[35–40] The electrochemical stability of Co–NC-750 °C was further studied by chronoamperometry. As can be seen from Figure 3c, after a continuous operation for 10 h at a constant overpotential of 330 mV (vs standard oxygen potential), the decayed current density of Co–NC-750 °C is ≈12% of the initial value compared to the 22% for Pt/C, demonstrating its high stability in the long-term cycling. As evidenced by Figure S8, Supporting Information, the Pt dissolution from carbon and the weak interaction of Pt/C with CC are responsible for the degradation in ORR performance of Pt/C, whereas the close protection of NC on Co nanoparticles and the strong combination between Co–NC-750 °C and CC ensure a stable operation of Co–NC-750 °C during ORR. Such excellent ORR stability can also be revealed by a slight shift in the ORR polarization curve obtained after 10 000 cycles (Figure 3d), compared to that of the first cycle. As confirmed by XPS results (Figure S9, Supporting Information), more Co^{2+} species are reduced to metallic Co in the Co–NC-750 °C during the ORR process, accompanied by the generation of $Co(OH)_2$ and CoOOH. In addition, the polarization curves of Co–NC-750 °C at different rotating speeds were recorded, and then the Koutecky–Levich (K–L) plots were obtained from the corresponding curves (Figure S10, Supporting Information). It should be noted that the K–L plots do not show a good linearity at different potentials. This phenomenon could be attributed to the rough catalyst layer of Co–NC-750 °C caused by its high mass loading of active material and 3D porous array architecture, which actually change the electrode geometry and introduce significant turbulence when testing.[41] Therefore, the electron-transfer number (n) measured by the K–L method may not reflect the real catalytic behavior.

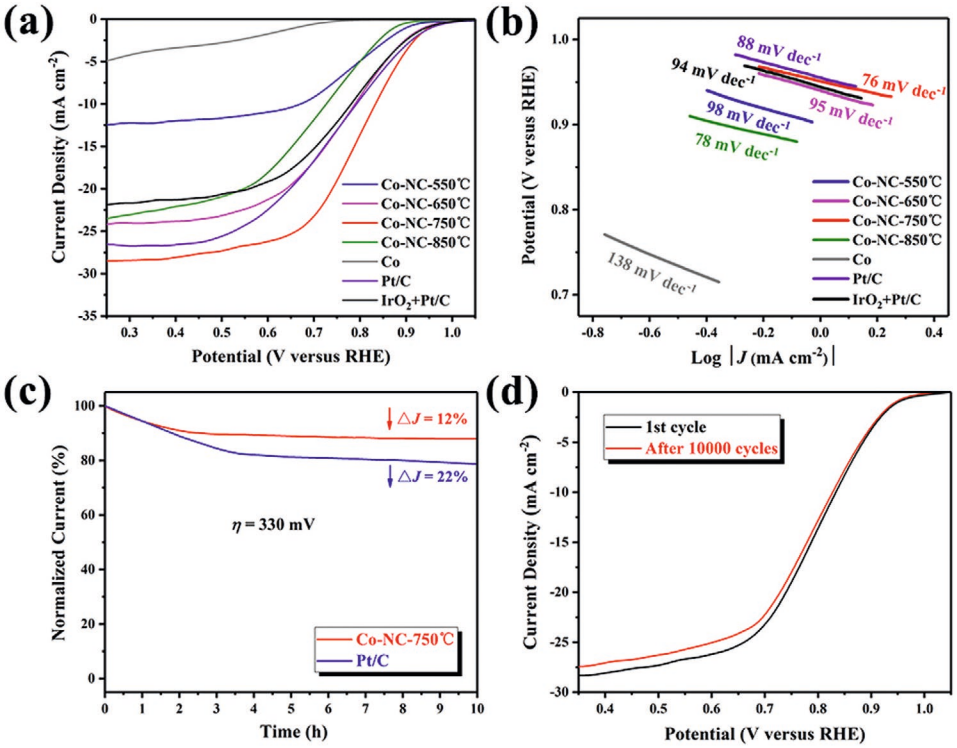

Figure 3. ORR electrocatalytic performance. a) Polarization curves of different electrocatalysts for ORR at 1600 rpm and b) the corresponding Tafel plots. c) Chronoamperometric response of Co–NC-750 °C and Pt/C at a constant overpotential of 330 mV versus standard oxygen potential. d) Polarization curves of Co–NC-750 °C before and after 10 000 potential sweeps between 0.4 and 1.0 V at 50 mV s^{-1}.

OER is the charging reaction on cathode of rechargeable metal–air batteries and the anode reaction in overall WSEs.[42] The electrocatalytic activity of the Co–NC electrocatalysts toward OER was also evaluated by LSV in 1 M KOH. As illustrated in **Figure 4**a, the Co–NC-750 °C exhibits highly electrocatalytic activity toward OER, which delivers a low overpotential of 240 mV (vs standard oxygen potential) to achieve a current density of 10 mA cm^{-2} (330 mV for IrO_2, 360 mV for metallic Co, and 335 mV for hybrid IrO_2 + Pt/C), and features a satisfactory OER faradaic efficiency of ≈99.06% at 1.68 V (Table S2, Supporting Information). Figure 4b displays that the Co–NC-750 °C possesses the lowest Tafel slope (87 mV dec^{-1}), significantly lower than those of IrO_2 (94 mV dec^{-1}), Co (132 mV dec^{-1}), and hybrid IrO_2 + Pt/C (99 mV dec^{-1}), further indicative of the superior kinetics of the Co–NC-750 °C toward OER. It is considered that the Co^{2+} species in Co–NC@CC favor OH^- adsorption regarding its high electrostatic affinity, while the Co–N_x and C–N species positively charged by electron-withdrawing NC can effectively facilitate the further adsorption of OH^-, synergistically accelerating the OER kinetics.[43–45] However, although the Co–NC-550 °C and Co–NC-650 °C feature numerous Co^{2+} species (the XPS result of Figure 2d) with high N contents (12.6 and 10.3 At%), they have poor conductivities as evidenced by the high electrical resistivities (443 and 313 mΩ cm^{-2}, respectively), exhibiting an unsatisfactory OER activity. And the Co–NC-850 °C also suffers from a sluggish OER kinetics despite the lowest electrical resistivity (155 mΩ cm^{-2}) but with a limited amount of Co^{2+} species and the lowest N content (6.7 At%). In comparison, the Co–NC-750 °C possesses a desirable content of Co^{2+} and N (9.1 At%) with a preferable conductivity (222 mΩ cm^{-2}), thus affording the best OER activity among the Co–NC@CC-series samples. Moreover, the Co–NC-750 °C delivers a satisfactory OER stability, which can be strongly confirmed by the chronoamperometric responses at a constant overpotential of 390 mV (vs standard oxygen potential) for 10 h. As shown in Figure 4c, ≈93% of the initial current density can be retained for the Co–NC-750 °C, whereas only 74% for IrO_2. The improved OER performance is ascribable to the formation of OER-active $Co(OH)_2$ and CoOOH,[8,46] which can be confirmed by the XPS results of Co–NC-750 °C before and after OER processes (with a detailed discussion presented in Figure S11, Supporting Information).

Apart from the excellent bifunctional ORR and OER performances, the Co–NC electrocatalysts also show an obvious promoting effect toward HER, the cathode reaction in WSE. As presented in Figure 4d, the Co–NC-750 °C exhibits the highest onset potential of –0.05 V among the Co–NC@CC-series samples, which is comparable to that of Pt/C (–0.01 V). Notably, it only requires a low overpotential of 73 mV (vs standard hydrogen potential) for a current density of 10 mA cm^{-2}, far below than most Co-based electrocatalysts reported in alkaline media.[8,9] Meanwhile, a high faradaic efficiency of Co–NC-750 °C can be determined, ≈99.39% at –0.32 V during the HER process (Table S2, Supporting Information). Furthermore, the excellent HER kinetics of Co–NC-750 °C is also supported by its low Tafel slope of ≈77 mV dec^{-1}, remarkably lower than that of Pt/C (87 mV dec^{-1}, Figure 4e). Such a favorable HER kinetics can also be attributed to the wonderful synergistic

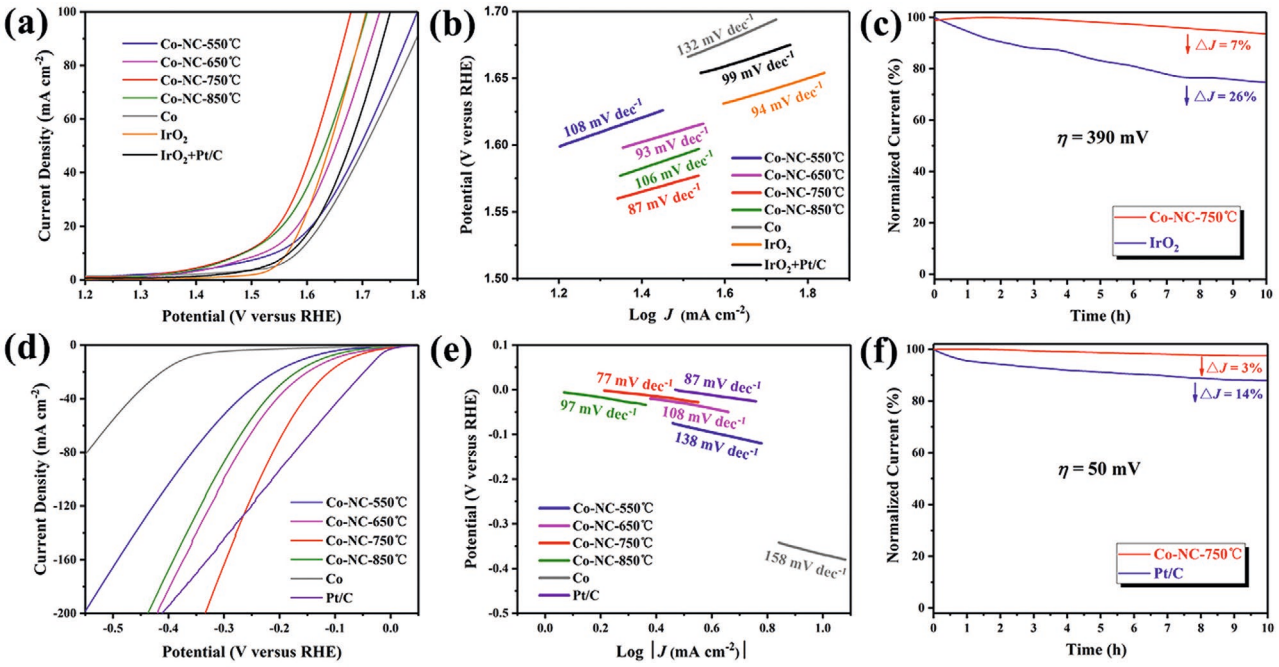

Figure 4. OER and HER electrocatalytic performances. a) Polarization curves of different electrocatalysts for OER at 1600 rpm and b) the corresponding Tafel plots. c) Chronoamperometric response of Co–NC-750 °C and IrO_2 at a constant overpotential of 390 mV versus standard oxygen potential. d) Polarization curves of different electrocatalysts for HER at 1600 rpm and e) the corresponding Tafel plots. f) Chronoamperometric response of Co–NC-750 °C and Pt/C at a constant overpotential of 50 mV versus standard hydrogen potential.

effect between mix-valent Co species. In particular, Co^0 has an appropriate binding energy for adsorbed H (H_{ads}), while Co^{2+} can be hydroxylated to dissociate H_2O, coboosting the elementary electrochemical reaction of HER ($H_2O + e^- = H_{ads} + OH^-$) in alkaline environment.[1,47–49] Notably, as shown in Figure 2d, the Co–NC-750 °C features a balanced ratio of Co^0 and Co^{2+} species (7.6%), comparable to Co–NC-550 °C (2.1%), Co–NC-650 °C (3.8%), and Co–NC-850 °C (21.7%), thus delivering the best HER kinetics among the Co–NC@CC-series samples. In addition, after a continuous operation of 10 h at a constant overpotential of 50 mV (vs standard hydrogen potential), Figure 4f illustrates that the current density of Co–NC-750 °C is well maintained with little attenuation (3% of its initial value), while an obvious current density loss is observed for Pt/C (14% of its initial value), indicating the excellent operational stability of Co–NC-750 °C toward HER.

The observed superior OER, ORR, and HER performances of Co–NC-750 °C could be fulfilled owing to the following factors. First, the high electrical conductivity of NC arrays with a hierarchical structure favors the transfer of reactants and electrons.[50–53] Second, the close protection of porous NC on these well-scattered Co nanoparticles can not only alleviate the aggregation of Co during different electrocatalytic processes, but provide abundant electroactive sites, excellent electrochemical stability, and electrical conductivity.[11,12,54] Third, by the coupling with NC, the configuration of mixed-covalent Co is further activated for OER, ORR, and HER, greatly driving its trifunctional electrocatalytic activities.[8,9,17] These satisfactory electrocatalytic performances are compared favorably to those multifunctional electrocatalysts reported recently (Table S3, Supporting Information), suggesting the as-prepared Co–NC electrocatalysts could be a highly efficient and cost-effective multifunctional electrocatalyst applied in the practical WSSs.

Giving the remarkable bifunctional OER and ORR catalytic properties of the Co–NC-750 °C, a rechargeable ZAB (abbreviated as Co–NC@CC ZAB) with a two-electrode configuration (Figure S12, Supporting Information) was assembled as an energy storage and output device for the WSS. Meanwhile, a ZAB based on hybrid IrO_2 + Pt/C electrocatalyst (abbreviated as IrO_2 + Pt/C ZAB) was also fabricated for comparison. As seen from Figure S13, Supporting Information, the Co–NC@CC ZAB presents an open circuit voltage of 1.650 V, which is higher than that of IrO_2 + Pt/C ZAB (1.551 V), confirming the outstanding electrocatalytic activity of Co–NC. When the ZABs are performed with discharging/charging test, the Co–NC@CC ZAB exhibits a smaller voltage gap, clearly indicative of a prominent charge–discharge reversibility (**Figure 5**a). Figure 5b displays the power–current density curves for aqueous ZABs, in which the maximum power density of Co–NC@CC ZAB (170 mW cm^{-2}) is higher than that of IrO_2 + Pt/C ZAB (140 mW cm^{-2}). Moreover, the Co–NC@CC ZAB yields a specific capacity of 792 mAh g^{-1}_{Zn} at a current density of 5 mA cm^{-2} (normalized by the total mass of Zn), far higher than that of IrO_2 + Pt/C ZAB (525 mAh g^{-1}_{Zn}) (Figure 5c), signaling an ultrahigh energy density of ≈1051 Wh kg^{-1}_{Zn}. The cycling tests in Figure 5d (charge and discharge for 10 min per cycle at 5 mA cm^{-2}) demonstrate that the Co–NC@CC ZAB exhibits a low voltage gap between discharge and charge (0.86 V) and a long operational time (725 h), compared with the 1.22 V and 352 h for IrO_2 + Pt/C ZAB, suggesting a high energy efficiency and superior cycling stability (Figure S14, Supporting Information). Evidently, such

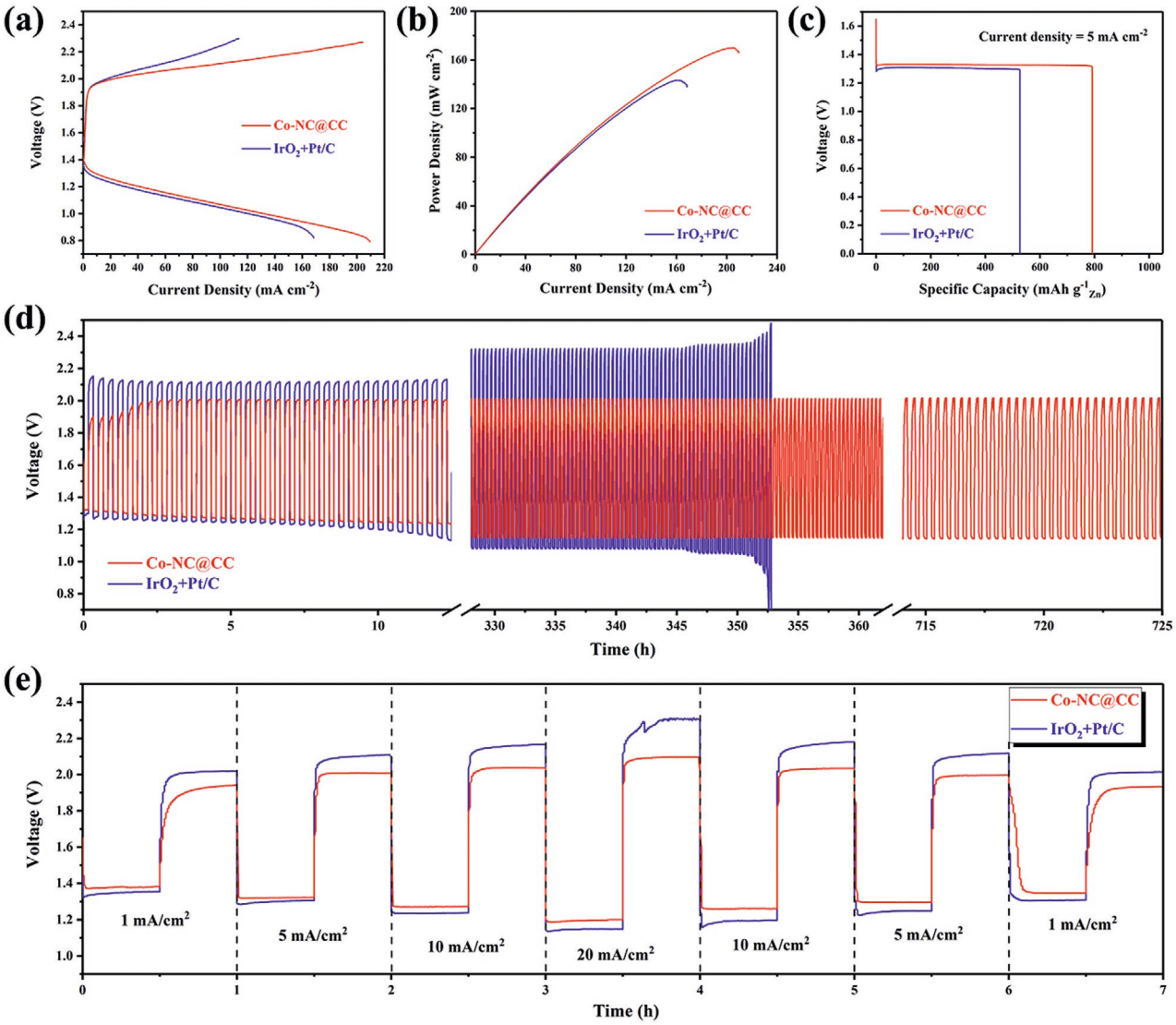

Figure 5. The electrochemical properties of ZABs. a) Charge and discharge polarization curves, b) power–current density curves, c) voltage–capacity curves, d) galvanostatic cycling curves at a current density of 5 mA cm^{-2}, and e) discharge and charge rate curves at various current densities of aqueous ZABs with air cathodes of Co–NC@CC and hybrid IrO_2 + Pt/C.

outstanding performances of the ZAB with Co–NC@CC as the cathode (Table S4, Supporting Information) can be well correlated to Co nanoparticles closely protected by NC and the potent combination between Co–NC and CC induced by the free-standing design.[55] To further assess the rechargeable ability of as-assembled ZABs, the discharge and charge rate tests were carried out at different current densities with a cutoff time of 1 h per cycle. Without the pre-activation of batteries, Figure 5e illustrates that the Co–NC@CC ZAB shows lower charging voltage and higher discharging platform than IrO_2 + Pt/C ZAB. The voltage gap between discharge and charge of the Co–NC@CC ZAB gradually increases from 0.54 to 0.89 V as the current density increased from 1 to 20 mA cm^{-2}, whereas IrO_2 + Pt/C ZAB dramatically increased from 0.62 to 1.17 V, indicating the excellent rate capability of the Co–NC@CC ZAB, which can also confirmed by electrochemical impedance spectroscopy results[56–60] (with a detailed discussion presented in Figure S15, Supporting Information).

Inspired by its outstanding electrocatalytic activity toward HER, we further explored the Co–NC@CC in an overall WSE constructed by symmetrical electrodes, whereas the WSE using the prepared IrO_2 and Pt/C electrodes as the anode and cathode, respectively, was also constructed for comparison. Because of the excellent bifunctional OER and HER activities of the Co–NC@CC, its WSE requires an input voltage of 1.57 V to achieve a current density of 10 mA cm^{-2}, which outperforms that of Pt/C and IrO_2 electrode (1.72 V) (**Figure 6**a). After the continuous operation of 20 h, the chronoamperometric and chronopotentiometric curves demonstrate that the Co–NC@CC electrode-based WSE exhibits a 21% decayed current density and an elevated voltage of 0.06 V based on its initial values (Figure 6b), far superior to those of IrO_2 and

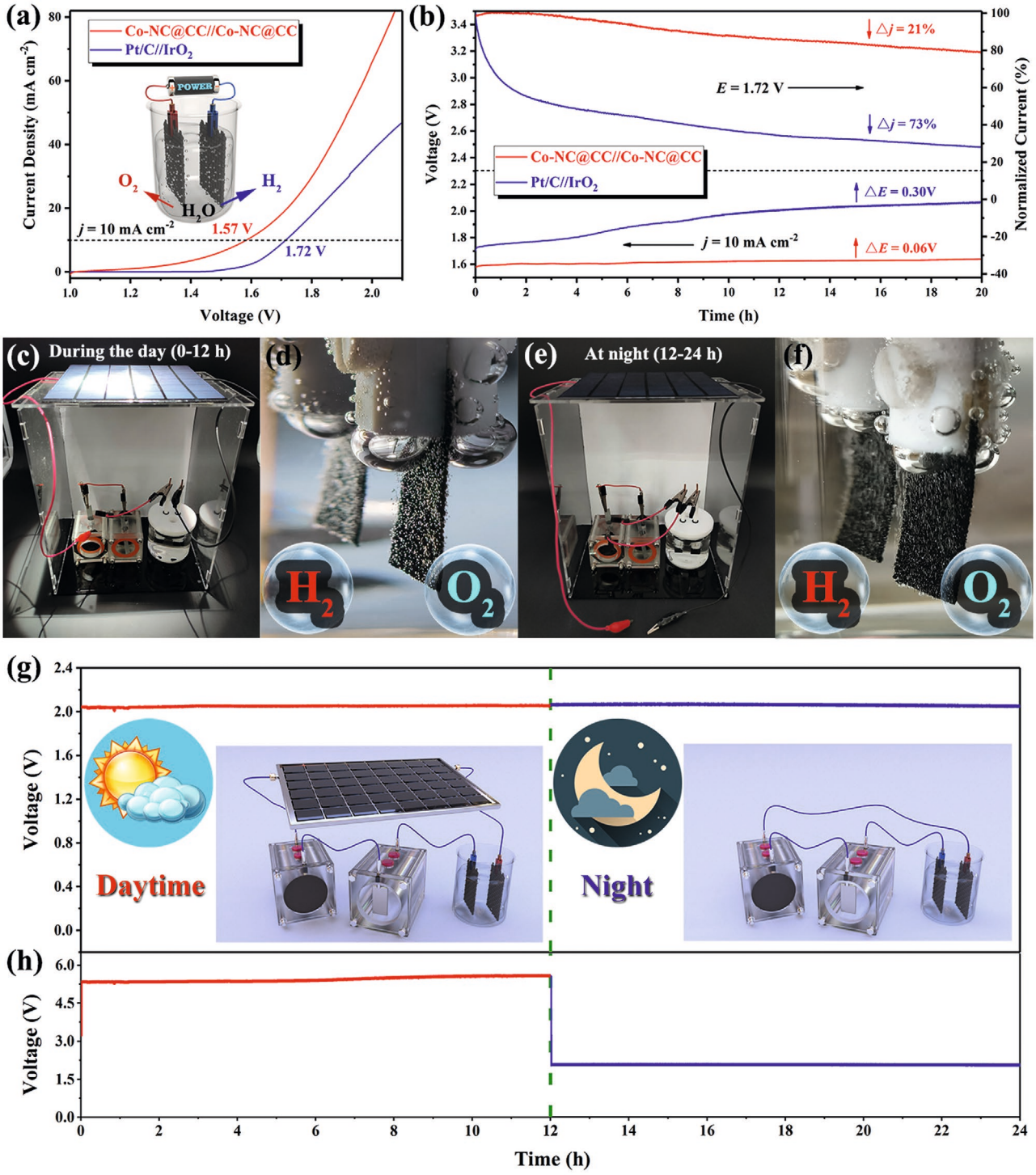

Figure 6. Solar-powered WSS performance during daytime and night. a) Polarization curves and b) chronopotentiometric and chronoamperometric curves of WSE constructed by two-electrode configuration. c,d) Photograph of the PSSP that simultaneously charges two-series ZABs and an overall WSE during the day, and e,f) the solar-charged ZABs subsequently drive the overall WSE at night. g) Voltage–time curves of overall water splitting powered by a PSSP (0–12 h) and two-series solar-charged ZABs (12–24 h). h) Charging curve of two-series ZABs charged by a PSSP (0–12 h) and discharging curve of the solar-charged ZABs during the driven process over water splitting.

Pt/C-based one (73% and 0.3 V). These results confirm that the symmetrical Co–NC@CC electrode configuration is efficient and durable for practical WSSs. In addition, considering its trifunctional electrocatalytic performance, we strategically integrated two-series Co–NC@CC ZABs (Figure S16a, Supporting Information, open circuit voltage of ≈3.179 V) with

the light-emitting diodes (LEDs) and an overall WSE based on symmetrical Co–NC@CC electrodes. As presented in Figure S16b, Supporting Information, the WSE and 75 red LEDs with "SCNU" shape are perfectly powered by the serial ZABs, and the vigorous generation of O_2 and H_2 bubbles are clearly observed on both Co–NC@CC electrodes at the same time (Figure S16c and Video S1, Supporting Information), emphasizing the high availability of the Co–NC@CC electrodes in practical WSSs.

To create solar-powered and uninterruptedly operating WSS, a novel WSS was constructed by integrating a PSSP, two-series rechargeable ZABs, and an overall WSE, in which the PSSP simultaneously charges the ZABs and the overall WSE during the day (Figure 6c), and the solar-charged ZABs subsequently drive the overall WSE at night (Figure 6e). As depicted in Figure S17a,b, Supporting Information, the commercial PSSP can deliver an open circuit voltage (V_{oc}) of ≈9.50 V under an optical power density of 1500 W m^{-2}. Figures 6g,h demonstrate voltage–time curves of the overall WSE and two-series ZABs over 24 h, respectively. The red line of Figure 6g,h shows that the PSSP provides a stable bias voltage of 2.05 V on the overall WSE and can also fully charge two-series ZABs during the day. At night, the overall WSE is powered by the as-obtained fully solar-charged ZABs and has a stable operating voltage of 2.06 V all night. Notably, the discharging curve of ZABs (blue line, Figure 6h) can be well maintained without interruptions or degradation, thus implying that our rechargeable ZABs can store enough solar energy for overall water splitting at night. In addition, as evidenced by Figure 6d,f and Video S2, Supporting Information, a substantial number of bubbles (O_2 and H_2) are continuously generated on both Co–NC@CC electrodes throughout day and night, indicating the uninterrupted operation of overall water splitting. These results confirm the successful fabrication of a solar-powered and uninterruptedly operating WSS, which can convert both solar and chemical energies into hydrogen energy throughout day and night.

In order to obtain the conversion efficiency of solar to H_2 (STH) for such solar-powered WSS, PSSP and Co–NC@CC-based WSE were combined as an integrated system for STH efficiency tests (the energy conversion efficiency of the Co–NC@CC-based ZABs is assumed to be 100%). As shown in Figure S17c,d, Supporting Information, the short circuit current (I_{sc}) of PSSP is 71 mA, and the WSE delivers an operating current (I_{op}) of 65 mA under the optical power density of 1500 W m^{-2}, corresponding to a high STH efficiency of 18.43% (with a detailed calculation presented in Figure S17, Supporting Information), which is comparable to previously reported values (Table S5, Supporting Information). Moreover, based on the real work conditions, the STH efficiency of this integrated system was also determined under the solar irradiation. Figure S18, Supporting Information, shows that this system exhibits a STH efficiency of ≈15.26% under a solar radiation density of 1024 W m^{-2} (Video S3, Supporting Information), calculated from the I_{sc} of PSSP (52 mA) and the I_{op} of WSE (40 mA). These performances place our as-designed system as one of the most cost-effective and energy-efficient solar-powered WSSs employing multifunctional Pt-free electrocatalysts.

3. Conclusions

In summary, we have developed a facile growth-carbonization synthetic route of the Co–NC multifunctional electrocatalyst for WSS, which shows remarkable trifunctional electrocatalytic activity and stability toward OER, ORR, and HER, significantly outperforming those of state-of-the-art Pt/C and IrO_2 electrocatalysts. The outstanding trifunctional electrocatalytic performances of Co–NC@CC are induced by the unique 3D porous array architecture with multiple electroactive sites and free-standing design, consequently resulting in the favorable reaction kinetics and mass transports. In addition, the close protection of NC on well-scattered Co nanoparticles, ensuring the excellent electrical conductivity and the electrochemical stability, further boosts trifunctional electrocatalytic performances. As a proof-of-concept application, a rechargeable ZAB assembled with the Co–NC@CC cathode exhibits a high open circuit potential of 1.63 V, an outstanding energy density of 1051 Wh kg^{-1}_{Zn} and an excellent cycling stability up to 725 h at a current density of 5 mA cm^{-2}. More significantly, an overall WSE constructed by symmetrical Co–NC@CC electrodes delivers a current density of 10 mA cm^{-2} at the low cell voltage of 1.57 V with a high stability, which is successfully integrated with the Co–NC@CC ZABs and a PSSP to create an uninterruptedly operating WSS, indicating the successful and practical application of the Co–NC electrocatalysts in solar-powered WSSs. Promisingly, this novel and fantastic strategy would be an alternative and efficient route to collect both solar and chemical energies in the form of hydrogen energy.

Supporting Information

Supporting Information is available from the Wiley Online Library or from the author.

Acknowledgements

This work was financially supported by National Natural Science Foundation of China (Grant no. 51471073).

Conflict of Interest

The authors declare no conflict of interest.

Data Availability Statement

Research data are not shared.

Keywords

efficient water splitting, electrolyzers, multifunctional electrocatalysts, zinc–air batteries

Received: November 17, 2020
Revised: February 6, 2021
Published online:

[1] J. N. Tiwari, N. K. Dang, S. Sultan, P. Thangavel, H. Y. Jeong, K. S. Kim, *Nat. Sustain.* **2020**, *3*, 556.
[2] Y. Zhang, S. Kumar, F. Marken, M. Krasny, E. Roake, S. Eslava, S. Dunn, E. D. Como, C. R. Bowen, *Nano Energy* **2019**, *58*, 183.
[3] C. Guan, X. Liu, A. M. Elshahawy, H. Zhang, H. Wu, S. J. Pennycook, J. Wang, *Nanoscale Horiz.* **2017**, *2*, 342.
[4] Z. Chen, X. Duan, W. Wei, S. Wang, B.-J. Ni, *Nano Energy* **2020**, *78*, 105270.
[5] X. Ren, H. Fan, C. Wang, J. Ma, H. Li, M. Zhang, S. Lei, W. Wang, *Nano Energy* **2018**, *50*, 562.
[6] Q. Zhang, B. He, L. Tang, Z. Zhou, L. Kang, J. Sun, T. Zhang, Q. Li, C. Li, J. Zhao, Z. Zhang, L. Wei, Y. Yao, *Adv. Funct. Mater.* **2019**, *29*, 1808889.
[7] J. Yin, Y. Li, F. Lv, M. Lu, K. Sun, W. Wang, L. Wang, F. Cheng, Y. Li, P. Xi, S. Guo, *Adv. Mater.* **2017**, *29*, 1704681.
[8] Z. Pei, Z. Tang, Z. Liu, Y. Huang, Y. Wang, H. Li, Q. Xue, M. Zhu, D. Tang, C. Zhi, *J. Mater. Chem. A* **2018**, *6*, 489.
[9] B. Tang, J. Yang, Z. Kou, L. Xu, H. L. Seng, Y. Xie, A. D. Handoko, X. Liu, Z. W. Seh, H. Kawai, H. Gong, W. Yang, *Energy Storage Mater.* **2019**, *23*, 1.
[10] L. Ma, S. Chen, Z. Pei, Y. Huang, G. Liang, F. Mo, Q. Yang, J. Su, Y. Gao, J. A. Zapien, C. Zhi, *ACS Nano* **2018**, *12*, 1949.
[11] C. Guan, A. Sumboja, H. Wu, W. Ren, X. Liu, H. Zhang, Z. Liu, C. Cheng, S. J. Pennycook, J. Wang, *Adv. Mater.* **2017**, *29*, 1704117.
[12] L. Zhu, D. Zheng, Z. Wang, X. Zheng, P. Fang, J. Zhu, M. Yu, Y. Tong, X. Lu, *Adv. Mater.* **2018**, *30*, 1805268.
[13] I. S. Amiinu, Z. Pu, X. Liu, K. A. Owusu, H. G. R. Monestel, F. O. Boakye, H. Zhang, S. Mu, *Adv. Funct. Mater.* **2017**, *27*, 1702300.
[14] X. Liu, W. Liu, M. Ko, M. Park, M. G. Kim, P. Oh, S. Chae, S. Park, A. Casimir, G. Wu, J. Cho, *Adv. Funct. Mater.* **2015**, *25*, 5799.
[15] J. Wu, H. Zhou, Q. Li, M. Chen, J. Wan, N. Zhang, L. Xiong, S. Li, B. Y. Xia, G. Feng, M. Liu, L. Huang, *Adv. Energy Mater.* **2019**, *9*, 1900149.
[16] D. Ji, L. Fan, L. Li, S. Peng, D. Yu, J. Song, S. Ramakrishna, S. Guo, *Adv. Mater.* **2019**, *31*, 1808267.
[17] K. Huang, R. Wang, S. Zhao, P. Du, H. Wang, H. Wei, Y. Long, B. Deng, M. Lei, B. Ge, H. Gou, R. Zhang, H. Wu, *Energy Storage Mater.* **2020**, *29*, 156.
[18] R. R. Hernandez, A. Armstrong, J. Burney, G. Ryan, K. Moore-O'Leary, I. Diédhiou, S. M. Grodsky, L. Saul-Gershenz, R. Davis, J. Macknick, D. Mulvaney, G. A. Heath, S. B. Easter, M. K. Hoffacker, M. F. Allen, D. M. Kammen, *Nat. Sustain.* **2019**, *2*, 560.
[19] H.-F. Wang, C. Tang, Q. Zhang, *Adv. Funct. Mater.* **2018**, *28*, 1803329.
[20] Z. Pen, J. Yu, Y. Li, C. Zhi, *Adv. Energy Mater.* **2018**, *8*, 1702467.
[21] Z. Pan, J. Yang, Q. Zhang, M. Liu, Y. Hu, Z. Kou, N. Liu, X. Yang, X. Ding, H. Chen, J. Li, K. Zhang, Y. Qiu, Q. Li, J. Wang, Y. Zhang, *Adv. Energy Mater.* **2019**, *9*, 1802753.
[22] Y. Xu, P. Deng, G. Chen, J. Chen, Y. Yan, K. Qi, H. Liu, B. Y. Xia, *Adv. Funct. Mater.* **2019**, *30*, 1906081.
[23] Y. Zhong, B. Li, S. Li, S. Xu, Z. Pan, Q. Huang, L. Xing, C. Wang, W. Li, *Nano-Micro Lett.* **2018**, *10*, 56.
[24] H.-F. Wang, C. Tang, B. Wang, B.-Q. Li, X. Cui, Q. Zhang, *Energy Storage Mater.* **2018**, *15*, 124.
[25] Y. Zeng, Z. Lai, Y. Han, H. Zhang, S. Xie, X. Lu, *Adv. Mater.* **2018**, *30*, 1802396.
[26] H. Yang, B. Wang, H. Li, B. Ni, K. Wang, Q. Zhang, X. Wang, *Adv. Energy Mater.* **2018**, *8*, 1801839.
[27] H.-F. Wang, C. Tang, B. Wang, B.-Q. Li, Q. Zhang, *Adv. Mater.* **2017**, *29*, 1702327.
[28] B.-Q. Li, S.-Y. Zhang, B. Wang, Z.-J. Xia, C. Tang, Q. Zhang, *Energy Environ. Sci.* **2018**, *11*, 1723.
[29] Z. Pei, J. Zhao, Y. Huang, Y. Huang, M. Zhu, Z. Wang, Z. Chen, C. Zhi, *J. Mater. Chem. A* **2016**, *4*, 12205.
[30] Z. Pan, H. Chen, J. Yang, Y. Ma, Q. Zhang, Z. Kou, X. Ding, Y. Pang, L. Zhang, Q. Gu, C. Yan, J. Wang, *Adv. Sci.* **2019**, *6*, 1900628.
[31] M. Hu, X. Li, J. Xiong, L. Zeng, Y. Huang, Y. Wu, G. Cao, W. Li, *Biosens. Bioelectron.* **2019**, *142*, 111594.
[32] X. Li, M. Hu, L. Zeng, J. Xiong, B. Tang, Z. Hu, L. Xing, Q. Huang, W. Li, *Biosens. Bioelectron.* **2019**, *145*, 111727.
[33] L. Lai, J. R. Potts, D. Zhan, L. Wang, C. K. Poh, C. Tang, H. Gong, Z. Shen, J. Lin, R. S. Ruoff, *Energy Environ. Sci.* **2012**, *5*, 7936.
[34] S. G. Peera, J. Balamurugan, N. H. Kim, J. H. Lee, *Small* **2018**, *14*, 1800441.
[35] M. Yu, Z. Wang, C. Hou, Z. Wang, C. Liang, C. Zhao, Y. Tong, X. Lu, S. Yang, *Adv. Mater.* **2017**, *29*, 1602868.
[36] J. Pan, Y. Y. Xu, H. Yang, Z. Dong, H. Liu, B. Y. Xia, *Adv. Sci.* **2018**, *5*, 1700691.
[37] Z. Pan, J. Yan, W. Zan, Z. Kou, C. Wang, X. Ding, C. Guan, T. Xiong, H. Chen, Q. Zhang, Y. Zhong, M. Liu, L. Xing, Y. Qiu, W. Li, C. Yan, Y. Zhang, J. Wang, *Energy Storage Mater.* **2019**, *23*, 375.
[38] X. Wang, Z. Liao, Y. Fu, C. Neumann, A. Turchanin, G. Nam, E. Zschech, J. Cho, J. Zhang, X. Feng, *Energy Storage Mater.* **2020**, *26*, 157.
[39] Z. Pan, J. Yang, J. Yang, Q. Zhang, H. Zhang, X. Li, Z. Kou, Y. Zhang, H. Chen, C. Yan, J. Wang, *ACS Nano* **2020**, *14*, 842.
[40] S. Y. Park, J.-S. Park, B. J. Kim, H. Lee, A. Walsh, K. Zhu, D. H. Kim, H. S. Jung, *Nat. Sustain.* **2020**, *3*, 1044.
[41] R. Zhou, Y. Zheng, M. Jaroniec, S.-Z. Qiao, *ACS Catal.* **2016**, *6*, 4720.
[42] Y. Yan, Y. Xu, B. Zhao, Y. Xu, Y. Gao, G. Chen, W. Wang, B. Y. Xia, *J. Mater. Chem. A* **2020**, *8*, 5070.
[43] J. Pan, X. L. Tian, S. Zaman, Z. Dong, H. Liu, H. S. Park, B. Y. Xia, *Batteries Supercaps* **2019**, *2*, 336.
[44] L. An, Y. Li, M. Luo, J. Yin, Y.-Q. Zhao, C. Xu, F. Cheng, Y. Yang, P. Xi, S. Guo, *Adv. Funct. Mater.* **2017**, *27*, 1703779.
[45] J. Yin, Y. Li, F. Lv, Q. Fan, Y.-Q. Zhao, Q. Zhang, W. Wang, F. Cheng, P. Xi, S. Guo, *ASC Nano* **2017**, *11*, 2275.
[46] Y. Li, Y. Liu, Q. Qian, G. Wang, G. Zhang, *Energy Storage Mater.* **2020**, *28*, 27.
[47] W. Sheng, M. Myint, J. G. Chen, Y. Yan, *Energy Environ. Sci.* **2013**, *6*, 1509.
[48] Y. Zheng, Y. Jiao, Y. Zhu, L. H. Li, Y. Han, Y. Chen, A. Du, M. Jaroniec, S. Z. Qiao, *Nat. Commun.* **2014**, *5*, 3783.
[49] L. Zhou, M. Shao, J. Li, S. Jiang, M. Wei, X. Duan, *Nano Energy* **2017**, *41*, 583.
[50] C. Guan, A. Sumboja, W. Zang, Y. Qian, H. Zhang, X. Liu, Z. Liu, D. Zhao, S. J. Pennycook, J. Wang, *Energy Storage Mater.* **2019**, *16*, 243.
[51] W. Qiu, Y. Li, A. You, Z. Zhang, G. Li, X. Lu, Y. Tong, *J. Mater. Chem. A* **2017**, *5*, 14838.
[52] Y. Zhong, Z. Pan, X. Wang, J. Yang, Y. Qiu, S. Xu, Y. Lu, Q. Huang, W. Li, *Adv. Sci.* **2019**, *6*, 1802243.
[53] C. Guan, W. Zhao, Y. Hu, Z. Lai, X. Li, S. Sun, H. Zhang, A. K. Cheetham, J. Wang, *Nanoscale Horiz.* **2017**, *2*, 99.
[54] Z. Pan, J. Yang, J. Jiang, Y. Qiu, J. Wang, *Mater. Today Energy* **2020**, *18*, 100523.
[55] H. Zhang, T. Wang, A. Sumboja, W. Zang, J. Xie, D. Gao, S. J. Pennycook, Z. Liu, C. Guan, J. Wang, *Adv. Funct. Mater.* **2018**, *28*, 1804846.
[56] X. Wang, H. Wang, M. Liu, W. Li, *Small* **2020**, *16*, 2000769.
[57] J. Chen, J. Vatamanu, L. Xing, O. Borodin, H. Chen, X. Guan, X. Liu, K. Xu, W. Li, *Adv. Energy Mater.* **2019**, *10*, 1902654.
[58] Q. Zhang, S. Liu, Z. Lin, K. Wang, M. Chen, K. Xu, W. Li, *Nano Energy* **2020**, *74*, 104860.
[59] Q. Zhang, K. Wang, X. Wang, Y. Zhong, M. Liu, X. Liu, K. Xu, W. Fan, L. Yu, W. Li, *ACS Appl. Mater. Interfaces* **2019**, *11*, 20854.
[60] Y. Huang, Z. Li, Z. Pei, Z. Liu, H. Li, M. Zhu, J. Fan, Q. Dai, M. Zhang, L. Dai, C. Zhi, *Adv. Energy Mater.* **2018**, *8*, 1802288.